

Thin Plate Spline Surface Reconstruction via the Method of Matched Sections

Igor Orynyak^a, Kirill Danylenko^a, Danylo Tavrov^{a,*}

^a*Applied Mathematics Department, National Technical University of Ukraine “Igor Sikorsky Kyiv Polytechnic Institute”, 37 Beresteiskyi Ave, Kyiv, 03056, Ukraine*

Abstract

This paper further develops the Method of Matched Sections (MMS), a robust numerical framework for the solution of boundary value problems governed by partial differential equations, specifically for surface modeling. While originating in mechanics, the method addresses critical challenges in isogeometric analysis and computer graphics by bridging the gap between physical accuracy and geometric continuity. By decomposing the domain into an assembly of 1D directional components matched along their entire boundaries, the method inherently enforces the continuity of all variational parameters, including second-order (curvature) and third-order (shear) derivatives. We demonstrate the method’s advanced capabilities in high-fidelity surface reconstruction and blending, showing that it consistently generates energetically optimal, fair surfaces even from complex boundary conditions or sparse internal points. By advancing the application of MMS, this research establishes it as a powerful, physics-informed geometric tool that satisfies the dual demands of rigorous numerical analysis and aesthetic computer-aided design.

Keywords: method of matched sections, physics-informed geometry, transfer matrix method, thin plate spline, boundary value problem, surface continuity

*Corresponding author

Email addresses: igor_orynyak@yahoo.com (Igor Orynyak),
k.a.danylenko@gmail.com (Kirill Danylenko), tavrov.danylo@111.kpi.ua (Danylo Tavrov)

1. Introduction

Constrained surface reconstruction is a fundamental problem in computer-aided design (CAD), computer graphics, and reverse engineering. The methodologies for addressing this problem can be broadly divided into two categories: purely geometric and physics-based [1].

The geometrical spline-based surfaces include Bézier, B-splines, and Non-Uniform Rational B-Splines (NURBS) surfaces. These are flexible and can be modified by controlling a set of parameters such as the order of basic functions, control points (number, positions, multiple vertices), and knot vectors (type, distances, multiple knot values, weights) [2]. They are very popular, and NURBS surfaces have become a standard in various industries for the digital representation and data exchange of geometric forms. Despite rapid advances in computational techniques, theoretical substantiation, and ready-to-use primitives, this traditional spline-based modeling can be difficult and counter-intuitive [3]. In such surface reconstruction methods, the resulting shapes often depend on the user’s heuristic skills and perceptions of users, leading to inconsistent representations for identical data [4]. The reason is that geometrical statements are often ill-posed, and additional criteria for the “fairness” of the surface are needed. Consequently, surface reconstruction can be considered a constrained optimal approximation problem in two dimensions, which requires a rigorous optimization procedure [5].

Variational techniques are used to optimize the shape of a surface by minimizing a specific energy functional, which often possesses clear physical analogues [6]. The thin-plate energy functional is mainly used to smooth the curvatures (minimize energy) of Bézier splines [7] and B-splines [8]. For the task of interpolation, this energy functional, E , minimized the aggregate curvature [5]:

$$E = \iint \left(\left(\frac{\partial^2 W}{\partial x^2} \right)^2 + 2 \left(\frac{\partial^2 W}{\partial x \partial y} \right)^2 + \left(\frac{\partial^2 W}{\partial y^2} \right)^2 \right) dx dy , \quad (1)$$

where W is the scalar field (surface elevation).

Direct physics-based methods have surged in popularity in recent years, especially in computer graphics, where their use has skyrocketed over the past few decades [9]. This is related to a demand for high-fidelity predictive simulations of real-life behavior [10]. Their significance is twofold: 1) they satisfy well-posed partial differential formulations from mathematical

physics; and 2) these functionals are considered the best for guaranteeing optimal surface fairness. The splines that originate from the elastic thin plate bending theory are very often considered optimal in this regard [5, 11]. Such surface splines are natural 2D extensions of 1D beam splines [12]. Similarly, 1D elastic beams provide both the technique of solution and the criteria for fairness [13, 14].

However, a critical distinction must be made. Like any boundary value problem, the solution must satisfy: a) the governing differential equation, b) internal constraints, and c) boundary conditions. The governing differential equation of the problem is the biharmonic equation:

$$\Delta^2 W(x, y) = q(x, y) , \quad (2)$$

where Δ is the Laplace operator, and $q(x, y)$ represents external data terms or constraints. The solution to (2) for $q(x, y) = 0$ automatically provides the minimum of the energy functional (1).

The term and technique of the thin plate spline (TPS) is very popular [15–17] it is often restricted to a linear combination of radial basis functions (RBFs) [18, 19]. These particular solutions, $W_r = A \cdot r^2 \ln r$, satisfy (2) everywhere except at constraint points, with r being the local radial distance r (counted with respect to the point of force application) and A an unknown constant related to the value of the force.

These functions might have some advantages over their counterparts, but they do not provide a solution to the boundary value problem, which additionally requires the general solution of the homogeneous equation (2). The problem with the application of the radial functions is that they lead to a dense matrix and therefore have a high computational cost. Furthermore, the problem may become ill-conditioned due to the global character of the thin-plate radial functions [20, 21]. The main drawback of the thin-plate radial function method, however, is its inability to account for constraints at the boundaries.

Therefore, it seems natural to resort to the experience gained in the theory of plates. There are two different approaches for the solution of (2) that account for constraints and boundaries: analytical and numerical. As is often the case, analytical solutions cannot be considered a universal technique. Their applications are restricted to narrower problems, for example, for blending (matching between known surfaces). An approach that provides analytical solutions to harmonic as well as biharmonic problems with

respect to some parametric surface coordinates u and v (PDE-based surface design) for simpler geometries was suggested in [22]. It was further enhanced for free-form surface generation for different boundary conditions, including periodic solutions [23]. This method has found applicability in the presentation of facial blendshapes [24], in the optimization design of head shapes for improving the aerodynamic performance of high-speed trains [25], and in the generation of optimal surfaces with curvature-level continuity under the constraint of feature curves for automotive styling design [3]. Yet the main question regarding the fairness of the generated surface remains open: Is the PDE-based design able to provide the best properties of the surface (1), accounting for the arbitrariness of the non-orthogonal parametric coordinates u and v ?

To address boundary constraints rigorously, we turn to numerical methods in Computational Mechanics (CM). The finite element method (FEM) was proposed for surface reconstruction [5]. As demonstrated in [12], the usual Ritz-based energy minimization approach with triangular elements is applied to derive the stiffness matrix and forcing vector. The combined use of smoothing techniques and mixed finite element techniques for the thin plate with the application of rectangular elements is given in [26].

Nevertheless, although the essence and governing equations for the thin plate model are the same for both CM and Computer Graphics (CG), they rarely interact in their methods and findings. A rare positive example is in 3D rod deformation, where some findings from the CG community [27] are also very popular in the CM world. Furthermore, a comparison between two groups of existing codes has demonstrated that CM codes sometimes (for the spatial rod) perform better than well-known reference models from Mechanical Engineering, yet CG thin plate design codes generally fail to pass some simple tests [28]. The CG community is still not eager to rely on the findings of CM, perhaps because their primary goals are different. Despite the declared need for accuracy, CG requires, first and foremost, the continuity of solutions, including the second derivatives (curvatures), everywhere within the body. For CM, the main goal is accuracy at specific points.

The main peculiarity of traditional FEM is clearly outlined in a series of works by Almeida et al. [29, 30]. In most, if not all, commercial FEM systems, the conforming formulation is used, which satisfies the constitutive relations and compatibility for the assumed displacement field. However, equilibrium is satisfied only in a weak sense; that is, “they are not in equilibrium with the body forces and do not have tractions that equilibrate with the

static boundary conditions and are not continuous between elements” [30]. The same is noted by the authors of [31], who emphasized that Newton’s third law is therefore violated at the boundaries between elements. But it is precisely the mechanical forces and moments in CM solutions that are proportional to the curvatures. Thus, while being accurate, they do not provide a plausible (continuous) picture of the body deformation.

In a geometric context, these “forces” and “moments” correspond directly to surface derivatives and curvatures. Thus, while FEM provides accurate displacements, it may fail to provide a C^2 -continuous (plausible) representation of the surface. To bridge the gap between CM and CG communities, one must prove that a numerical solution can accurately recover curvature (moments) and enforce high-order continuity. It is worth demonstrating that a biharmonic function can be restored within the whole area by the FE solution based only on the specified boundary conditions, generated by this biharmonic function. It is also necessary to demonstrate that the application of the boundary conditions generated by an arbitrary function leads to the FE solution, whose value of the functional (1) is less than the respective value of (1) related to this function.

The recently proposed Method of Matched Sections (MMS), as a universal multiphysical numerical technique [32–35], possesses both accuracy and continuity for functions and their higher derivatives. This paper demonstrates that MMS serves as a robust engine for optimal surface reconstruction. The demonstration of this ability is the goal of the present paper. Due to the novelty of our approach, we restrict ourselves to an initially rectangular domain meshed by rectangular elements. This is not a principal restriction of the method, and the successful treatment of curvilinear boundaries by triangular elements was demonstrated in [35]. We show the following capabilities:

- Accurate recovery of the analytical solution under point constraints.
- Restoration of biharmonic functions under varied boundary conditions.
- When boundary conditions are taken from an arbitrary function, the restored function possesses the best energy-minimizing property.
- Reconstruction of fair surfaces from sparse internal data points.

The rest of this paper is structured as follows. Section 2 provides a brief overview of the Method of Matched Sections as applied to thin plate bending, detailing the analytical relations and the matrix formulation. Section

3 presents a series of numerical examples, demonstrating the method’s accuracy in handling point constraints, its effectiveness in surface blending for both symmetric and non-symmetric biharmonic functions, and its ability to reconstruct surfaces from sparse internal data points. Finally, Section 4 concludes the paper with a summary of the key findings and their implications.

2. Thin Plate Bending By MMS

The problem statement follows the formulation in [32, 33]. MMS reduces Partial Differential Equations (PDEs) to a system of Ordinary Differential Equations (ODEs) via a semi-analytical decomposition. The 2D problem is treated as a coupled system of 1D equations along orthogonal directions. Here, we present the solution in a form compatible with the Transfer Matrix Method (TMM) [32, 36].

2.1. Analytical Relations and Parameters Mapping

Consider the rectangular element shown in Fig. 1, with dimensions a and b . All parameters and their positive directions are shown. For geometric applications, the Poisson’s ratio ν , which couples orthogonal deformations, is set to 0 to represent a pure minimization of the geometric functional.

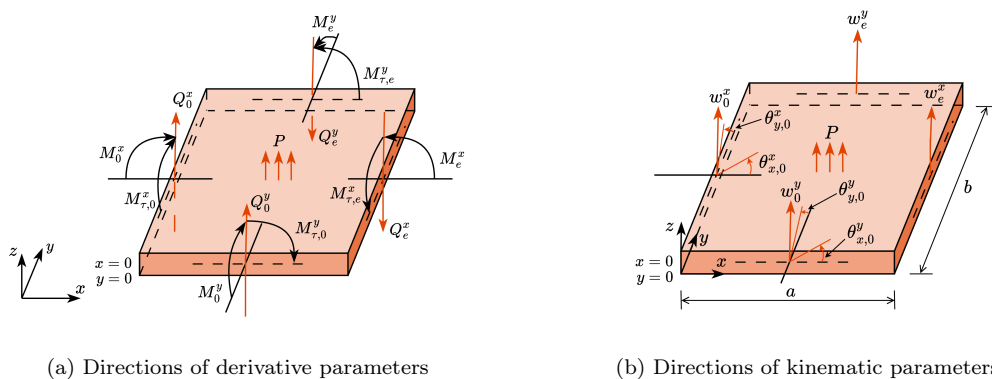


Figure 1: General scheme of a finite element decomposition

The surface element is decomposed into two 1D directional components: the X-section (along $y = b/2$) and the Y-section (along $x = a/2$). The X-section is characterized by 6 parameters, which depend only on x and are related to the central line of this beam ($x, b/2$). They are:

- surface elevation (transverse displacement $w^x(x)$);
- normal first order derivative, or normal slope (angle of rotation of the beam $\theta_n^x(x)$);
- tangent first order derivative, or angle of twisting $\theta_\tau^x(x)$;
- distributed moments applied to the X -section: $M_n^x(x)$ (principal curvature parameter, or bending moment) and $M_\tau^x(x)$ (twisting curvature parameter, or twisting moment);
- third-order derivative, or distributed transverse force $Q^x(x)$.

Analogously, the Y -section is characterized by 6 parameters, which depend only on y and pertain to its central line $(a/2, y)$, namely, $w^y(y)$, $\theta_n^y(y)$, $\theta_\tau^y(y)$, $M_n^y(y)$, $M_\tau^y(y)$, and $Q^y(y)$. The superscripts are used to indicate the plane the parameters are related to.

These 12 parameters are coupled via the differential equations shown and solved in [32]. For completeness, we will provide these solutions here.

The dependencies of the parameters along the central lines are as follows. For the third derivatives along x :

$$Q^x(x) = Q_0^x + A_1x , \quad (3)$$

where the subscript 0 the initial section, so $Q_0^x = Q^x(0)$. For the third derivative $Q^y(y)$ along y :

$$Q^y(y) = Q_0^y + (P - A_1)y , \quad (4)$$

where P is the distributed data term (or external load). In geometrical applications, it can be used to account for given geometrical constraints. For the twisting second derivatives:

$$M_\tau^y(y) = M_{\tau,0}^y + A_2y , \quad (5)$$

$$M_\tau^x(x) = M_{\tau,0}^x + A_3x . \quad (6)$$

For the bending second derivatives:

$$M_n^x(x) = M_{n,0}^x + Q_0^x x + \frac{A_1 x^2}{2} - A_2 x , \quad (7)$$

$$M_n^y(y) = M_{n,0}^y + Q_0^y y + \frac{(P - A_1) y^2}{2} - A_3 y . \quad (8)$$

The integrally averaged curvature parameters are:

$$M_{n,\text{avg}}^x = \frac{1}{a} \int_0^a M_n^x(x) dx = M_{n,0}^x + \frac{Q_0^x a}{2} + \frac{A_1 a^2}{6} - \frac{A_2 a}{2}, \quad (9)$$

$$M_{n,\text{avg}}^y = \frac{1}{b} \int_0^b M_n^y(y) dy = M_{n,0}^y + \frac{Q_0^y b}{2} + \frac{(P - A_1) b^2}{6} - \frac{A_3 b}{2}. \quad (10)$$

From the geometric equations for the twist angles:

$$\theta_\tau^x(x) = \theta_{\tau,0}^x + \frac{M_{\tau,0}^x}{D(1-\nu)} x + \frac{A_3}{D(1-\nu)} \frac{x^2}{2}, \quad (11)$$

$$\theta_\tau^y(y) = \theta_{\tau,0}^y + \frac{M_{\tau,0}^y}{D(1-\nu)} y + \frac{A_2}{D(1-\nu)} \frac{y^2}{2}. \quad (12)$$

The solutions for slope angles are given by:

$$\begin{aligned} \theta_n^x(x) &= \theta_{n,0}^x + \frac{1}{D(1-\nu^2)} \left(M_{n,0}^x x + \frac{Q_0^x x^2}{2} + \frac{A_1 x^3}{6} - \frac{A_2 x^2}{2} \right) \\ &\quad - \frac{\nu}{D(1-\nu^2)} M_{n,\text{avg}}^y \cdot x, \end{aligned} \quad (13)$$

$$\begin{aligned} \theta_n^y(y) &= \theta_{n,0}^y + \frac{1}{D(1-\nu^2)} \left(M_{n,0}^y y + \frac{Q_0^y y^2}{2} + \frac{(P - A_1) y^3}{6} - \frac{A_3 y^2}{2} \right) \\ &\quad - \frac{\nu}{D(1-\nu^2)} M_{n,\text{avg}}^x \cdot y. \end{aligned} \quad (14)$$

Integration yields the surface elevation functions:

$$\begin{aligned} w^x(x) &= w_0^x + \theta_{n,0}^x x + \frac{1}{D(1-\nu^2)} \left(\frac{M_{n,0}^x x^2}{2} + \frac{Q_0^x x^3}{6} + \frac{A_1 x^4}{24} - \frac{A_2 x^3}{6} \right) \\ &\quad - \frac{\nu}{D(1-\nu^2)} M_{n,\text{avg}}^y \cdot \frac{x^2}{2}, \end{aligned} \quad (15)$$

$$\begin{aligned} w^y(y) &= w_0^y + \theta_{n,0}^y y + \frac{1}{D(1-\nu^2)} \left(\frac{M_{n,0}^y y^2}{2} + \frac{Q_0^y y^3}{6} + \frac{(P - A_1) y^4}{24} - \frac{A_3 y^3}{6} \right) \\ &\quad - \frac{\nu}{D(1-\nu^2)} M_{n,\text{avg}}^x \cdot \frac{y^2}{2}. \end{aligned} \quad (16)$$

2.2. Matrix Equations and Algorithm

To solve the system, we determine the auxiliary constants A_1, A_2, A_3 via compatibility conditions at the element center. We require the ‘‘welding’’ of

the two directional components, ensuring continuity of elevation and slope:

$$w^x \left(\frac{a}{2} \right) = w^y \left(\frac{b}{2} \right) , \quad (17)$$

$$\theta_n^x \left(\frac{a}{2} \right) = \theta_\tau^y \left(\frac{b}{2} \right) , \quad (18)$$

$$\theta_\tau^x \left(\frac{a}{2} \right) = \theta_n^y \left(\frac{b}{2} \right) . \quad (19)$$

These equations effectively substitute the PDE with a coupled ODE system. The relationship between constants and the state vector \mathbf{Z}_0 (the 12 boundary parameters) is expressed as:

$$\begin{pmatrix} A_1 \\ A_2 \\ A_3 \end{pmatrix} = \begin{pmatrix} \alpha_{1,1} & \alpha_{1,2} & \dots & \alpha_{1,11} & \alpha_{1,12} \\ \alpha_{2,1} & \alpha_{2,2} & \dots & \alpha_{2,11} & \alpha_{2,12} \\ \alpha_{3,1} & \alpha_{3,2} & \dots & \alpha_{3,11} & \alpha_{3,12} \end{pmatrix} \begin{pmatrix} Z_{1,0} \\ \vdots \\ Z_{12,0} \end{pmatrix} + P \begin{pmatrix} \beta_1 \\ \beta_2 \\ \beta_3 \end{pmatrix} , \quad (20)$$

where all coefficients $\alpha_{i,j}$ and β_i are known. For convenience, we renumber all 12 initial conditions as a state vector \mathbf{Z}_0 :

$$w_0^x = Z_{1,0} , \quad \theta_{n,0}^x = Z_{2,0} , \quad \theta_{\tau,0}^x = Z_{3,0} , \quad (21)$$

$$M_{n,0}^x = Z_{4,0} , \quad M_{\tau,0}^x = Z_{5,0} , \quad Q_0^x = Z_{6,0} , \quad (22)$$

$$w_0^y = Z_{7,0} , \quad \theta_{n,0}^y = Z_{8,0} , \quad \theta_{\tau,0}^y = Z_{9,0} , \quad (23)$$

$$M_{n,0}^y = Z_{10,0} , \quad M_{\tau,0}^y = Z_{11,0} , \quad Q_0^y = Z_{12,0} . \quad (24)$$

Then it is possible to separately compile the equations for all six parameters that characterize the X -section for any $x = \text{const}$. They can be formally presented as:

$$\begin{pmatrix} Z_1(x) \\ \vdots \\ Z_6(x) \end{pmatrix} = \begin{pmatrix} a_{1,1}(x) & \dots & a_{1,12}(x) \\ \vdots & \ddots & \vdots \\ a_{6,1}(x) & \dots & a_{6,12}(x) \end{pmatrix} \begin{pmatrix} Z_{1,0} \\ \vdots \\ Z_{12,0} \end{pmatrix} + P \begin{pmatrix} b_{P,1}(x) \\ \vdots \\ b_{P,6}(x) \end{pmatrix} , \quad (25)$$

where $Z_1(x) = w^x(x)$ and so on. The coefficients are such that $a_{m,m}(0) = 1$, and all other coefficients are equal to zero at point $x = 0$, i.e. $a_{m,k}(0) = 0$, and all $b_{P,m}(0) = 0$.

For the six parameters that characterize the state of the Y -section, it can be written by analogy:

$$\begin{pmatrix} Z_7(y) \\ \vdots \\ Z_{12}(y) \end{pmatrix} = \begin{pmatrix} c_{1,1}(y) & \dots & c_{1,12}(y) \\ \vdots & \ddots & \vdots \\ c_{6,1}(y) & \dots & c_{6,12}(y) \end{pmatrix} \begin{pmatrix} Z_{1,0} \\ \vdots \\ Z_{12,0} \end{pmatrix} + P \begin{pmatrix} d_{P,1}(y) \\ \vdots \\ d_{P,6}(y) \end{pmatrix}, \quad (26)$$

where $Z_7(y) = w^y(y)$ and so on. The coefficients are such that $c_{m,m+6}(0) = 1$, and all other coefficients are equal to zero at point $y = 0$, i.e. $c_{m,k}(0) = 0$, and all $d_{P,m}(0) = 0$.

According to the logic of TMM, it is convenient to formally specify a set of 12 auxiliary unknown constants (to be eliminated at the further steps of the calculation process), which are the values of the main parameters of the two 1D components at their ends. For the X -section ($x = a$):

$$\begin{pmatrix} Z_{13} \\ \vdots \\ Z_{18} \end{pmatrix} = \begin{pmatrix} a_{1,1}(a) & \dots & a_{1,12}(a) \\ \vdots & \ddots & \vdots \\ a_{6,1}(a) & \dots & a_{6,12}(a) \end{pmatrix} \begin{pmatrix} Z_{1,0} \\ \vdots \\ Z_{12,0} \end{pmatrix} + P \begin{pmatrix} b_{P,1}(a) \\ \vdots \\ b_{P,6}(a) \end{pmatrix}, \quad (27)$$

where $Z_{13} = w^x(x = a) \equiv w_e^x$ and so on, with the subscript e meaning the value of the specific parameter at the end of the section.

For the Y -section ($y = b$), we have:

$$\begin{pmatrix} Z_{19} \\ \vdots \\ Z_{24} \end{pmatrix} = \begin{pmatrix} c_{1,1}(b) & \dots & c_{1,12}(b) \\ \vdots & \ddots & \vdots \\ c_{6,1}(b) & \dots & c_{6,12}(b) \end{pmatrix} \begin{pmatrix} Z_{1,0} \\ \vdots \\ Z_{12,0} \end{pmatrix} + P \begin{pmatrix} d_{P,1}(b) \\ \vdots \\ d_{P,6}(b) \end{pmatrix}, \quad (28)$$

where $Z_{19} = w^y(y = b) \equiv w_e^y$ and so on.

Equations (25) and (26) are usually termed field transfer matrix (FTM) equations [36], which give the solution at any point x or y by knowing the state at the initial (inlet) point. When the considered points are the outlet points (upper or right sides) of the plate, equations (27) and (28) give the relation of the state in them with the inlet parameters.

The above connection equations (27) and (28) relate to a single element. In this case, we have 24 unknowns (Z_1 – Z_{24}), which are related by 12 connection equations. They must be supplemented by 3 boundary conditions at each of the 4 sides. Thus, the total number of unknowns is 24, which is equal to the number of equations.

For a multi-element mesh, we need to provide continuity at the borders between elements. If elements n_1 and n_2 share a boundary, designated as j_1 and j_2 respectively, then their vectors of state must match:

$$\mathbf{Z}_{i,j_1}^{n_1} = \mathbf{Z}_{i,j_2}^{n_2}, \quad 1 \leq i \leq 6. \quad (29)$$

This provides 6 conjugation equations (in TMM terms, a point transfer matrix [36]). Each side of an element can thus contain either 3 boundary equations or 3 conjugation equations; overall, the number of boundary or conjugation equations is 12. Thus, each element has 24 unknown parameters for which 12+12 equations exist, so the problem can be solved. This enforces C^2 continuity or higher (depending on the solved variables), which is a distinct advantage over standard C^0 or C^1 FEM approaches.

3. Numerical Validation and Surface Reconstruction

To evaluate the method's geometric efficiency, we calculate the discrete energy integral

$$E \approx \sum_{n=1}^N E_n, \quad (30)$$

where

$$E_n = \left(\left(M_n^x \left(\frac{a_n}{2} \right) \right)^2 + \left(M_\tau^x \left(\frac{a_n}{2} \right) \right)^2 + \left(M_\tau^y \left(\frac{b_n}{2} \right) \right)^2 + \left(M_n^y \left(\frac{b_n}{2} \right) \right)^2 \right) \times (a_n \cdot b_n), \quad (31)$$

where E_n is the element energy contribution based on the squared curvature parameters.

3.1. Constraint Handling: The Corner-Supported Surface

We first consider a canonical validation case: a cantilevered square domain with two adjacent corners supported (fixed to zero elevation) (Fig. 2). This tests the method's ability to handle singular geometric constraints.

The MMS enables flexible implementation of corner constraints. We compare three formulations (Fig. 3):

- *MMS-B*: zero elevation at boundary centers;

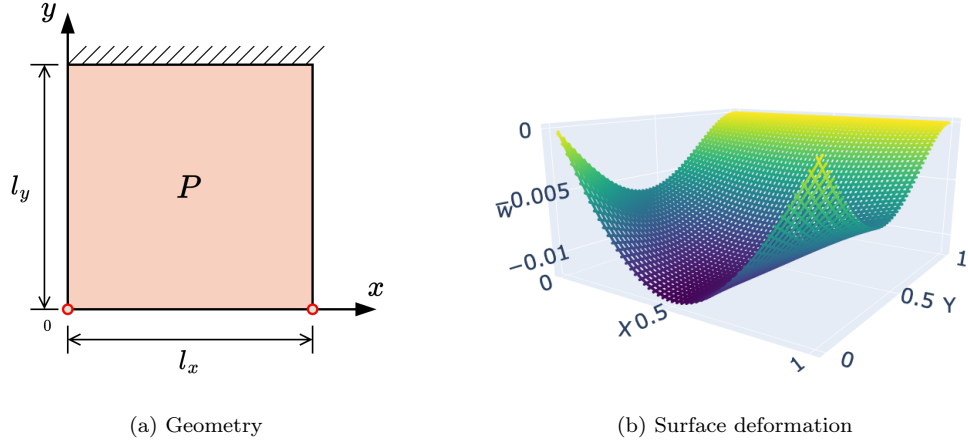


Figure 2: Square domain with singular corner constraints

- *MMS-BA*: incorporating tangential slope constraints;
- *MMS-BAM*: incorporating slope and curvature/moment constraints.

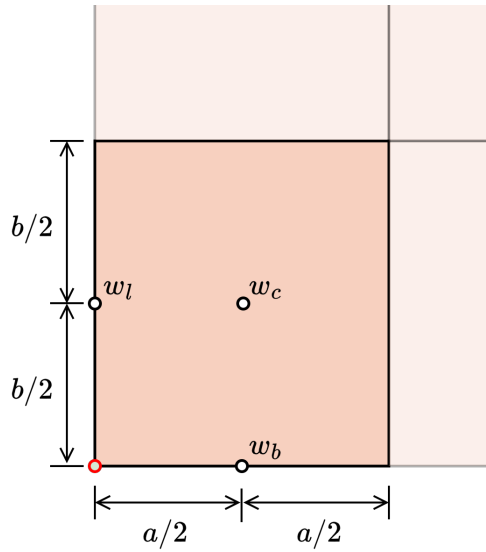


Figure 3: Corner element topology

For the thin plate problem, MMS requires 3 boundary conditions per side. The first approach (MMS-B) involves setting fixed elevations at the center

of the boundary side. For the left and lower sides, this gives:

$$w_0^x = Z_1 = 0, \quad M_{n,0}^x = Z_4 = 0, \quad M_{\tau,0}^x = Z_5 = 0, \quad (32)$$

$$w_0^y = Z_7 = 0, \quad M_{n,0}^y = Z_{10} = 0, \quad M_{\tau,0}^y = Z_{11} = 0. \quad (33)$$

The second approach (MMS-BA) considers the tangential angles at the boundary fixation. Taking into account that the position in the corner point is given, we can write for the left-lower point:

$$w_0^x - \theta_{\tau,0}^x \cdot \frac{b}{2} = 0, \quad w_0^y - \theta_{\tau,0}^y \cdot \frac{a}{2} = 0. \quad (34)$$

This leads to the following boundary conditions:

$$Z_1 - Z_3 \frac{b}{2} = 0, \quad Z_4 = 0, \quad Z_5 = 0, \quad (35)$$

$$Z_7 - Z_9 \frac{a}{2} = 0, \quad Z_{10} = 0, \quad Z_{11} = 0. \quad (36)$$

In the third approach (MMS-BAM), we also simulate the variational effect of a concentrated Lagrange multiplier at the corner. Assuming we have distributed tangential second derivative and third derivative, we calculate the resulting moment at the corner point and equate it to zero:

$$M_{\tau,0}^x b - Q_0^x b \frac{b}{2} = 0, \quad M_{\tau,0}^y a - Q_0^y a \frac{a}{2} = 0. \quad (37)$$

This yields the following equations for each side:

$$Z_1 - Z_3 \frac{b}{2} = 0, \quad Z_4 = 0, \quad Z_5 - Z_6 \frac{b}{2} = 0, \quad (38)$$

$$Z_7 - Z_9 \frac{a}{2} = 0, \quad Z_{10} = 0, \quad Z_{11} - Z_{12} \frac{a}{2} = 0. \quad (39)$$

Table 1 compares the results against high-precision reference solutions from [37]. Evidently, the third approach gives the best results, but they are still far from the accurate ones.

To further refine the result near the singularity, we can either use a much denser mesh or apply local meshing, for example, by resorting to our merging and division procedure [32]. We use a simplified approach instead by applying a linear reduction to several boundary rows of elements, as shown in Fig. 4 (where the first and last 4 rows are reduced so that the symmetry of the grid is preserved and all the key points fall on the MMS skeleton lines). This scaling allows us to specify corner boundary conditions much more accurately, improving the overall accuracy without increasing global computation cost (Table 2).

Table 1: Comparison for square domain with singular corner constraints for different MMS approaches ($\nu = 0.3$, mesh: 171×171)

Approach	$\frac{DW\left(\frac{l_x}{2}, \frac{l_y}{2}\right)}{ql_x^4}$	$\frac{M_x\left(\frac{l_x}{2}, \frac{l_y}{2}\right)}{ql_x^2}$	$\frac{M_y\left(\frac{l_x}{2}, \frac{l_y}{2}\right)}{ql_x^2}$	$\frac{DW\left(\frac{l_x}{4}, \frac{l_y}{2}\right)}{ql_x^4}$	$\frac{M_x\left(\frac{l_x}{4}, \frac{l_y}{2}\right)}{ql_x^2}$	$\frac{M_y\left(\frac{l_x}{4}, \frac{l_y}{2}\right)}{ql_x^2}$
MMS-B	0.007936	0.035962	0.050924	0.007280	0.027425	0.054210
MMS-BA	0.008026	0.037794	0.049389	0.007293	0.028897	0.052624
MMS-BAM	0.008064	0.037878	0.049415	0.007328	0.028983	0.052667
Exact [37]	0.008052	0.037900	0.049495	0.007316	0.029028	0.052692

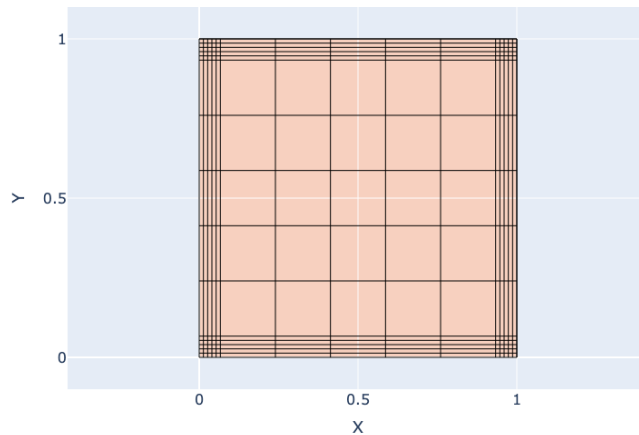


Figure 4: 15×15 mesh with boundary scaling

3.2. Surface Blending With Cosine-Like Biharmonic Patches

A key advantage of MMS over traditional splines is its robust handling of boundary conditions, allowing us to effectively solve blending problems and obtain the most energy-efficient surfaces. We demonstrate this by solving the blending problem for a cosine-like biharmonic function (Fig. 5):

$$\begin{aligned}
 W(x, y) = & \cos(x) \left(\frac{1}{2} \cosh(y) - \coth\left(\frac{\pi}{2}\right) \frac{y}{\pi} \sinh(y) \right) \\
 & + \cos(y) \left(\frac{1}{2} \cosh(x) - \coth\left(\frac{\pi}{2}\right) \frac{x}{\pi} \sinh(x) \right), \tag{40}
 \end{aligned}$$

which is constructed to be zero at the boundaries $x = \pm\pi/2$ and $y = \pm\pi/2$, and equal to 1 at the center.

Table 2: Comparison for square domain with singular corner constraints for MMS-BAM approach using boundary scaling ($\nu = 0.3$, mesh: 251×251)

y	x	DW/ql_x^4		M_x/ql_x^2		M_y/ql_x^2	
		Exact [37]	MMS	Exact [37]	MMS	Exact [37]	MMS
0	$0.25l_x$	0.008098	0.008102	0.076216	*0.076467	0	0
	$0.5l_x$	0.011237	0.011241	0.094329	*0.094558	0	0
$0.25l_y$	0	0.005163	0.005165	0	0	0.071900	*0.072110
	$0.25l_x$	0.008934	0.008937	0.050837	0.050839	0.056157	0.056152
	$0.5l_x$	0.010596	0.010598	0.066909	0.066911	0.052390	0.052379
$0.5l_y$	0	0.005797	0.005798	0	0	0.062840	*0.062970
	$0.25l_x$	0.007316	0.007317	0.029028	0.029024	0.052692	0.052686
	$0.5l_x$	0.008052	0.008053	0.037900	0.037898	0.049495	0.049488

Values marked with an asterisk (*) are taken from the nearest available skeleton line.

To solve this problem in MMS, we set the boundary conditions at the midpoints of the outer sides of the boundary elements. We set the elevation w , normal angle θ_n , and tangential angle θ_τ . Elevation w is set to the value of function (40) at the boundary points. The angular boundary conditions are specified according to the first derivatives:

$$\begin{aligned}
 \theta_n^x &= \theta_\tau^y = \frac{\partial W}{\partial x} \\
 &= -\sin(x) \left(\frac{1}{2} \cosh(y) - \coth\left(\frac{\pi}{2}\right) \frac{y}{\pi} \sinh(y) \right) \\
 &\quad + \cos(y) \left(\frac{1}{2} \sinh(x) - \coth\left(\frac{\pi}{2}\right) \frac{1}{\pi} \sinh(x) - \coth\left(\frac{\pi}{2}\right) \frac{x}{\pi} \cosh(x) \right), \quad (41)
 \end{aligned}$$

$$\begin{aligned}
 \theta_n^y &= \theta_\tau^x = \frac{\partial W}{\partial y} \\
 &= \cos(x) \left(\frac{1}{2} \sinh(y) - \coth\left(\frac{\pi}{2}\right) \frac{1}{\pi} \sinh(y) - \coth\left(\frac{\pi}{2}\right) \frac{y}{\pi} \cosh(y) \right) \\
 &\quad - \sin(y) \left(\frac{1}{2} \cosh(x) - \coth\left(\frac{\pi}{2}\right) \frac{x}{\pi} \sinh(x) \right). \quad (42)
 \end{aligned}$$

Table 3 demonstrates rapid convergence. Precise results are obtained even when using only $7 \cdot 7 = 49$ elements. Crucially, the reconstructed surface exhibits near-perfect energy characteristics. For a 71×71 mesh, we get $E_{\text{Exact}} = 17.1850$ and $E_{\text{MMS}} = 17.1785$.

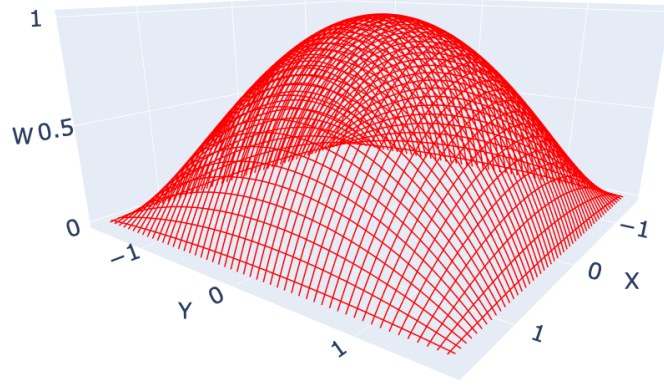


Figure 5: Cosine-like biharmonic surface patch

Table 3: Cosine-like biharmonic surface restoration from boundary elevations and angles

$M \times N$	$w^x(0, 0)$	$\theta^x(0, 0)$	$M^x(0, 0)$	$w^x(\pi/3, 0)$	$\theta^x(\pi/3, 0)$	$M^x(\pi/3, 0)$
7×7	0.9973	0.0000	0.6934	0.5952	0.8213	1.0125
21×21	0.9997	0.0000	0.6940	0.5960	0.8232	1.0156
31×31	0.9999	0.0000	0.6941	0.5960	0.8234	1.0146
71×71	1.0000	0.0000	0.6941	0.5961	0.8235	1.0147
Exact	1	0	0.6941	0.5961	0.8236	1.0147

We then reconstruct the same surface using higher-order boundary data, i.e. second derivatives (curvatures) at the boundaries:

$$\begin{aligned}
M_n^x = \frac{\partial^2 W}{\partial x^2} = & -\cos(x) \cdot \left(\frac{\cosh(y)}{2} - \coth\left(\frac{\pi}{2}\right) \cdot \frac{y \sinh(y)}{\pi} \right) \\
& + \cos(y) \cdot \left(\frac{\cosh(x)}{2} - 2 \coth\left(\frac{\pi}{2}\right) \cdot \frac{\cosh(x)}{\pi} - \coth\left(\frac{\pi}{2}\right) \cdot \frac{x \sinh(x)}{\pi} \right),
\end{aligned} \tag{43}$$

$$\begin{aligned}
M_n^y = \frac{\partial^2 W}{\partial y^2} = & -\cos(y) \cdot \left(\frac{\cosh(x)}{2} - \coth\left(\frac{\pi}{2}\right) \cdot \frac{x \sinh(x)}{\pi} \right) \\
& + \cos(x) \cdot \left(\frac{\cosh(y)}{2} - 2 \coth\left(\frac{\pi}{2}\right) \cdot \frac{\cosh(y)}{\pi} - \coth\left(\frac{\pi}{2}\right) \cdot \frac{y \sinh(y)}{\pi} \right).
\end{aligned} \tag{44}$$

Instead of setting tangential angles, we set the values for tangential curvatures:

$$\begin{aligned}
M_\tau^x &= M_\tau^y = \frac{\partial^2 W}{\partial x \partial y} \\
&= -\sin(x) \cdot \left(\frac{\sinh(y)}{2} - \coth\left(\frac{\pi}{2}\right) \cdot \frac{\sinh(y)}{\pi} - \coth\left(\frac{\pi}{2}\right) \cdot \frac{y \cosh(y)}{\pi} \right) \\
&\quad - \sin(y) \cdot \left(\frac{\sinh(x)}{2} - \coth\left(\frac{\pi}{2}\right) \cdot \frac{\sinh(x)}{\pi} - \coth\left(\frac{\pi}{2}\right) \cdot \frac{x \cosh(x)}{\pi} \right).
\end{aligned} \tag{45}$$

The comparison results in Table 4 show accurate convergence even for these specific boundary conditions. The energy functional for the 71×71 grid is $E_{\text{MMS}} = 17.1821$, which corresponds to an extremely smooth bi-harmonic function.

Table 4: Cosine-like biharmonic surface restoration from boundary elevations and second derivatives

$M \times N$	$w^x(0, 0)$	$\theta^x(0, 0)$	$M^x(0, 0)$	$w^x(\pi/3, 0)$	$\theta^x(\pi/3, 0)$	$M^x(\pi/3, 0)$
7×7	1.0062	0.0000	0.6996	0.6004	0.8288	1.0211
21×21	1.0008	0.0000	0.6948	0.5966	0.8242	1.0167
31×31	1.0004	0.0000	0.6944	0.5963	0.8238	1.0152
71×71	1.0001	0.0000	0.6942	0.5961	0.8236	1.0148
Exact	1	0	0.6941	0.5961	0.8236	1.0147

3.3. Blending With Non-Symmetric Biharmonic Surfaces

We consider a more complex, asymmetrical function in the domain $[0; \pi/2] \times [-\pi; \pi]$ (Fig. 6):

$$W(x, y) = \left(\frac{\pi}{2} - x \right) e^{3x} \cos(3y). \tag{46}$$

By analogy with the previous example, we set the values of the function and its first derivatives at the boundaries. The first derivatives are:

$$\theta_n^x = \theta_\tau^y = \frac{\partial W}{\partial x} = \left(\frac{3\pi}{2} - 3x - 1 \right) e^{3x} \cos(3y), \tag{47}$$

$$\theta_n^y = \theta_\tau^x = \frac{\partial W}{\partial y} = -3 \left(\frac{\pi}{2} - x \right) e^{3x} \sin(3y). \tag{48}$$

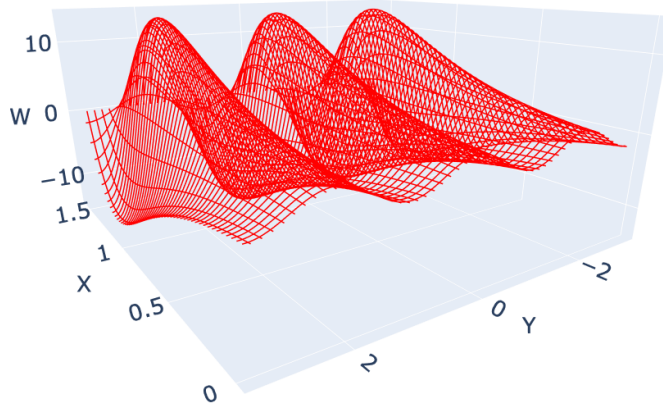


Figure 6: Non-symmetric biharmonic surface

Table 5 shows that a larger number of elements is required to obtain high-precision results, but a smooth surface can be constructed even with the smallest mesh. For a 251×251 grid, the energy functionals are $E_{\text{Exact}} = 233228.4505$ and $E_{\text{MMS}} = 233201.0544$.

Table 5: Restoration of biharmonic function (46) from its boundary elevations and angles

$M \times N$	$w^x(\pi/4, 0)$	$\theta^x(\pi/4, 0)$	$M^x(\pi/4, 0)$	$w^x(3\pi/8, 0)$	$\theta^x(3\pi/8, 0)$	$M^x(3\pi/8, 0)$
21×21	8.1251	14.1549	11.9868	13.3142	6.3979	83.1234
51×51	8.2612	14.2841	11.3837	13.4350	6.1488	84.2887
101×101	8.2801	14.3026	11.3018	13.4523	6.1148	84.4478
251×251	8.2855	14.3078	11.2788	13.4572	6.1053	84.4930
Exact	8.2865	14.3088	11.2743	13.4581	6.1035	84.5016

Specifying the boundaries with elevation and second derivatives (Table 6) yields an energy functional of $E_{\text{MMS}} = 233192.9470$ for the 251×251 grid. Thus, MMS allows for extremely flexible ways to specify boundary conditions and effectively solves the problem of blending with smooth surfaces.

3.4. Cosine-Based Surface With Input Points

We now address surface reconstruction from sparse internal data points (interpolation). Let us consider constructing surfaces based on boundary as

Table 6: Restoration of biharmonic function (46) from its boundary elevations and curvatures

$M \times N$	$w^x(\pi/4, 0)$	$\theta^x(\pi/4, 0)$	$M^x(\pi/4, 0)$	$w^x(3\pi/8, 0)$	$\theta^x(3\pi/8, 0)$	$M^x(3\pi/8, 0)$
21×21	8.0376	14.0985	11.9612	13.2100	6.4043	82.5687
51×51	8.2485	14.2773	11.3828	13.4206	6.1511	84.2140
101×101	8.2770	14.3010	11.3017	13.4488	6.1155	84.4296
251×251	8.2850	14.3076	11.2788	13.4566	6.1055	84.4901
Exact	8.2865	14.3088	11.2743	13.4581	6.1035	84.5016

well as internal input points. We will demonstrate the smoothness and precision of the resulting splines by restoring a surface generated by a twice continuously differentiable, but non-biharmonic, function in the interval $x, y \in [-\pi/2; \pi/2]$ (Fig. 7):

$$W(x, y) = \cos(x) \cdot \cos(y). \quad (49)$$

The energy of this surface is $E_{\text{Exact}} = \pi^2 \approx 9.8696$.

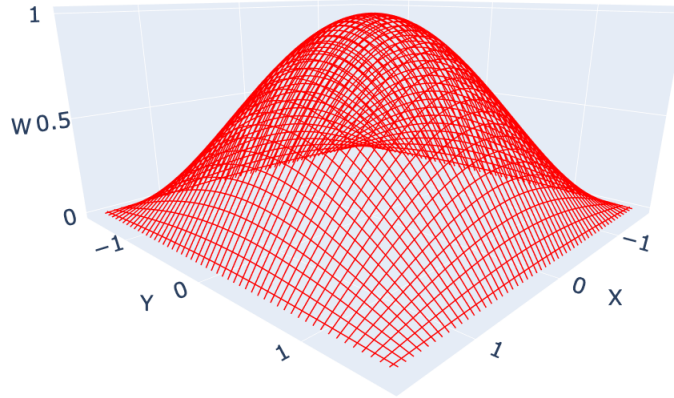


Figure 7: Cosine-based surface

First, we restore the surface using only boundary conditions (elevations and first derivatives), like in the previous examples. In particular, the first derivatives are:

$$\begin{aligned} \theta_n^x = \theta_\tau^y &= \frac{\partial W}{\partial x} = -\sin(x) \cdot \cos(y), \\ \theta_n^y = \theta_\tau^x &= \frac{\partial W}{\partial y} = -\cos(x) \cdot \sin(y). \end{aligned}$$

For a small 11×11 grid, the maximum elevation is 0.6431, far from the original's central value of 1 (Fig. 8). However, its energy, $E_{\text{MMS}} = 6.9089$, is significantly lower (better) than the original surface's energy. The energy obtained for MMS in this case has an additional error due to averaging over large elements. Unlike a cosine-based function, the surface constructed by MMS is bi-harmonic and therefore has the optimal energy characteristics given the boundary conditions. However, the surfaces do not match well.

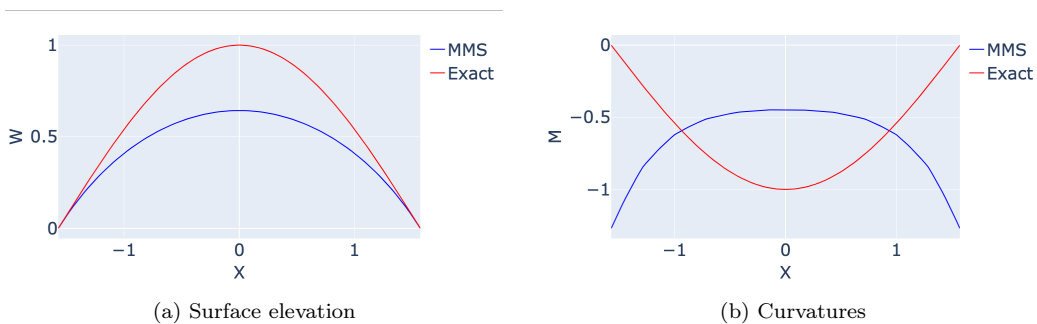


Figure 8: Cosine-based results along the line $y = 0$ (11×11 , no inputs)

It should be noted that the energy degraded not only because of the stronger bend in the center, but also because any deviation from MMS (which satisfies the biharmonic equation) will ultimately result in a lower quality surface. Substituting the condition $W = 0.3$ (lower than for the biharmonic functions, i.e. 0.6431) in the center, we still get worse energy: $E_{\text{MMS}} = 8.9159$.

To match the original surface, we introduce a constraint at the central point, $W(0, 0) = 1$. The elevation now matches the original, but the energy has increased to $E_{\text{MMS}} = 9.3161$ (Fig. 9). Although the obtained surface is quite close to the original, certain calculations require a much denser mesh. On a finer 251×251 grid, a third derivative discontinuity develops at the central point (Fig. 10). Indeed, constraining w at the center engenders third derivative Q in this element, which introduces a large gradient of the third derivative between the constrained element and its unconstrained neighbors. This behavior corresponds to the general property of the thin plate particular solution, where the second derivative contains a singularity.

In our case, the concentrated force is spreading over the element, so the larger the element, the smaller the peak of the second derivative. Despite

this, the total surface energy remains at the same level $E_{\text{MMS}} = 9.3145$, which is still better than the original surface energy.

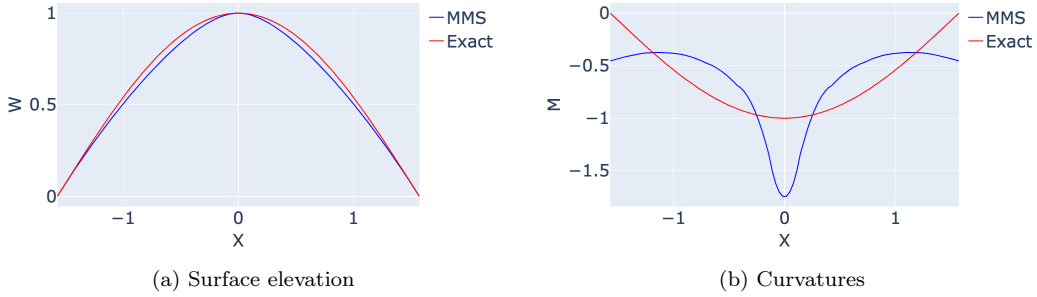


Figure 9: Cosine-based results along the line $y = 0$ (11×11 , central input)

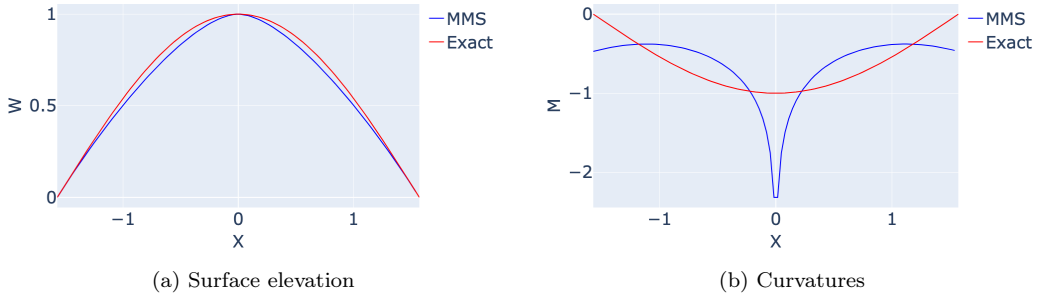


Figure 10: Cosine-based results along the line $y = 0$ (251×251 , central input)

To mitigate this and produce visually fair surfaces for graphics applications, we introduce a regularization technique. We distribute the variational constraint over adjacent elements using a smoothing kernel α :

$$\alpha = \frac{1}{1 + \left(\frac{d}{\zeta \cdot \min(l_x, l_y)}\right)^2}, \quad (50)$$

where d is the distance to the attachment point, and ζ is a regularization parameter. The kernel α is set to zero if the distance between the element centers exceeds $d > \frac{\min(l_x, l_y)}{5}$.

By adjusting the regularization parameter and the maximum distance for a specific problem, one can significantly improve the accuracy of surface reconstruction and smooth the curvature discontinuity near attachment points,

while the surface energy still surpasses that of the original surface in quality. For example, by taking $\zeta = 50$, the results are improved, while the surface energy remains practically unchanged: $E_{\text{MMS}} = 9.5280$ (Fig. 11).

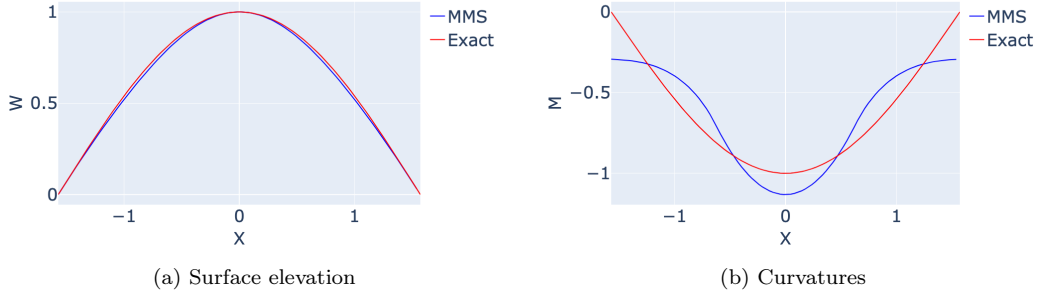


Figure 11: Cosine-based results along the line $y = 0$ (251×251 , central input, $\zeta = 50$)

We can also exclude regularization by either setting the second part of the denominator (50) to zero or assuming ζ to be very large. Doing so will give us the best approximation for the case of central input (Fig. 12).

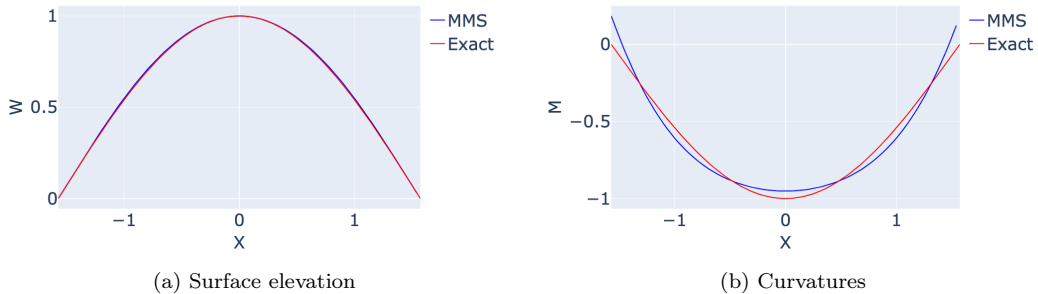


Figure 12: Cosine-based results along the line $y = 0$ (251×251 , central input, $\zeta = 10^6$)

We also demonstrate that the third derivative discontinuity arises only in the vicinity of the attachment point. Going back to the example shown in Fig. 10, if the bending curvatures are taken along an off-center skeleton line $y = 0.25$ instead of the central line $y = 0$, the distribution becomes considerably smoother even without the regularization technique, as shown in Fig. 13.

Another important advantage of MMS is its ability to operate with an irregular set of input points. Suppose we are given 5 input points chosen

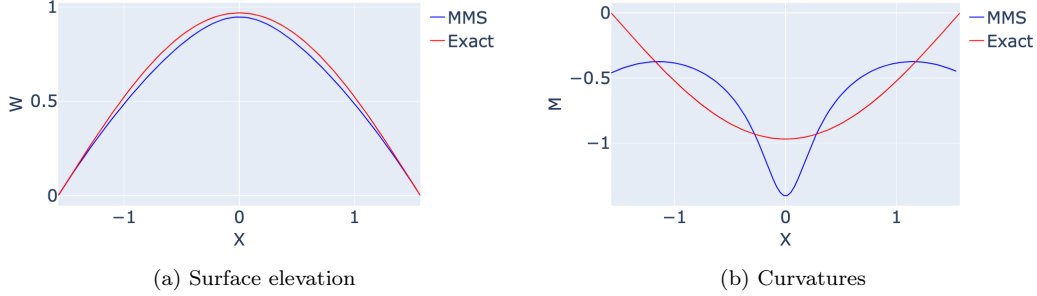


Figure 13: Cosine-based results along the line $y = 0.25$ (251×251 , central input, without regularization)

randomly; for convenience, we will align them with the centers of certain elements:

$$\left(\frac{20\pi}{251}, \frac{20\pi}{251}\right); \left(\frac{40\pi}{251}, \frac{80\pi}{251}\right); \left(-\frac{90\pi}{251}, \frac{70\pi}{251}\right); \left(-\frac{30\pi}{251}, -\frac{80\pi}{251}\right); \left(-\frac{60\pi}{251}, -\frac{20\pi}{251}\right) \quad (51)$$

From the results shown in Fig. 14, even with such an asymmetric set of points, the restoring quality remains very high, while the surface energy still outperforms that of the original surface: $E_{\text{MMS}} = 9.5445$.

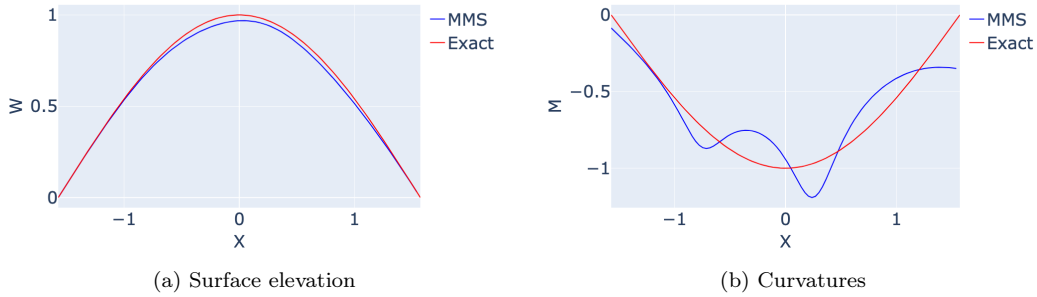


Figure 14: Cosine-based results along the line $y = 0$ (251×251 , 5 inputs, without regularization)

We can also “spread” the load from the elements containing the input points (Fig. 15). The resulting energy is $E_{\text{MMS}} = 9.7271$.



Figure 15: Cosine-based results along the line $y = 0$ (251×251 , 5 input, $\zeta = 50$)

3.5. Complex Multi-Peak Reconstruction

Let us consider a much more complex surface, devoid of symmetries, taken from [38] and defined in the region $[-3; 3] \times [-4; 4]$ (Fig. 16):

$$W(x, y) = 3(1 - x)^2 e^{-x^2 - (y+1)^2} - 10 \left(\frac{1}{5}x - x^3 - y^5 \right) e^{-x^2 - y^2} - \frac{1}{3} e^{-(x+1)^2 - y^2}. \quad (52)$$

It has three local minima and three local maxima near $(0, 0)$, and at the boundaries, the function and its derivatives vanish. The energy functional for this surface is $E_{\text{Exact}} = 4161.9368$.

Using a 251×251 grid and 6 entry points at the local extrema, we can approximate the original surface quite accurately (Fig. 17), with the approximate coordinates being $(0, 1.59)$, $(-0.45, -0.64)$, $(1.29, 0)$, $(0.24, -1.63)$, $(-1.34, 0.19)$, $(0.29, 0.32)$. From an energy perspective, the resulting surface is of much higher quality, $E_{\text{MMS}} = 2731.5228$. Applying the regularization technique significantly smooths the third derivatives near the attachment points, though it increases the energy to $E_{\text{MMS}} = 3112.1235$ (Fig. 18).

Adding 9 more random points (for a total of 15) with regularization significantly improves the reconstruction accuracy, while the surface energy approaches the original: $E_{\text{MMS}} = 3920.1770$ (Fig. 19).

4. Conclusion

While computational mechanics and computer graphics share roots in the physics of thin plates, their numerical objectives often diverge. CM often prioritizes nodal accuracy, whereas CG demands global smoothness and curvature continuity. This paper bridges these fields using the Method of Matched

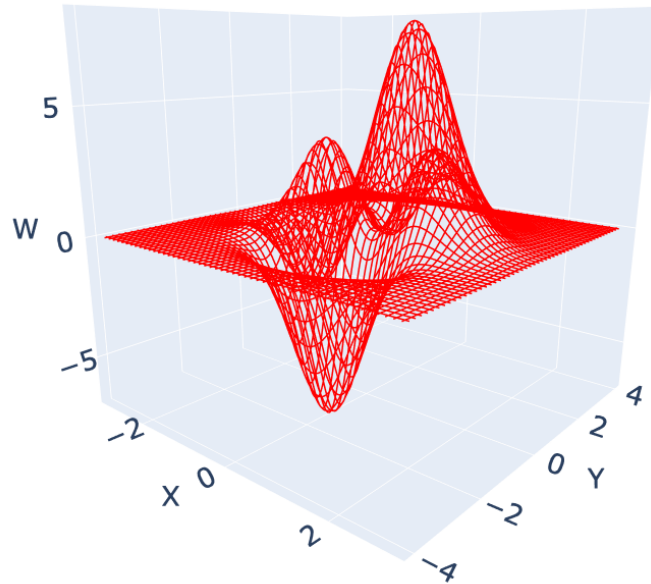


Figure 16: Multipeak surface

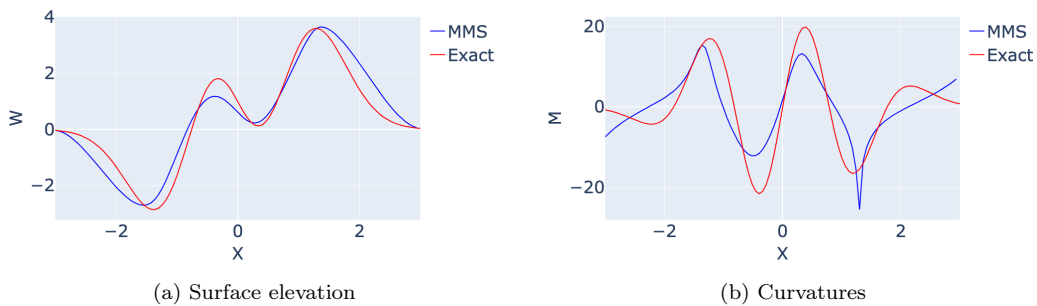


Figure 17: Multipeak results along the line $y = 0$ (251×251 , 6 inputs)

Sections. Unlike standard conforming Finite Element Method, which may violate higher-order continuity at element boundaries, MMS results in a visually plausible representation, suitable for graphics applications.

We demonstrated that MMS:

1. Successfully incorporates corner constraints and point data into the variational formulation. As demonstrated with the example of a point-supported surface, this novel approach to handling concentrated con-



Figure 18: Multippeak results along the line $y = 0$ (251×251 , 6 inputs, $\zeta = 50$)

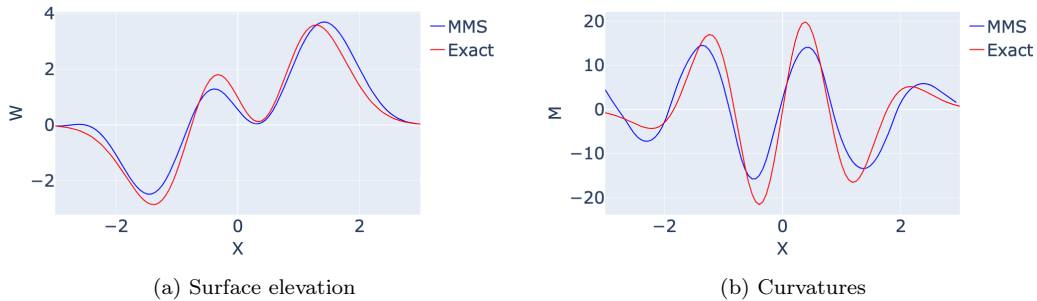


Figure 19: Multippeak results along the line $y = 0$ (251×251 , 15 inputs, $\zeta = 50$)

straints led to a significant improvement in accuracy. This capability is a key step in reconciling the discrete nature of mechanical constraints with the continuity requirements of computer graphics.

2. Accurately reconstructs surfaces from diverse boundary data (derivatives of 1st or 2nd order). Numerical examples show rapid and precise convergence to the exact surface, confirming that our mathematical formulation is ideally suited for surface blending tasks where seamless continuity between different patches is paramount.
3. Generates surfaces that are inherently biharmonic and energetically optimal, surpassing the fairness of the generating functions. When boundary conditions are derived from an arbitrary, non-biharmonic function, the surface generated by our method is inherently biharmonic. This resulting surface is not only smooth but also energetically optimal, possessing a lower thin-plate energy value than the original function from which the boundaries were taken. If an internal measurement

point is added as a constraint, the reconstructed surface becomes geometrically closer to the original generating surface. Even in this constrained state, the surface's energy characteristics remain superior to those of the original, demonstrating an intrinsic tendency towards the smoothest possible shape that honors the given data.

4. Through a local regularization kernel, the method smooths curvature singularities induced by point constraints, ensuring visual quality for design applications. This approach successfully restores the continuity of curvatures while only marginally increasing the total surface energy, offering a practical way to regularize the solution for visual fairness.

Credit authorship contribution statement

Igor Orynyak: Conceptualization, Methodology, Writing – original draft.
Kirill Danylenko: Software, Validation, Visualization, Writing – review & editing.
Danylo Tavrov: Validation, Writing – review & editing.

Declaration of competing interest

The authors declare that they have no known competing relationships that could have appeared to influence the work reported in this paper.

References

- [1] J. M. Zheng, K. W. Chan, I. Gibson, Constrained deformation of freeform surfaces using surface features for interactive design, *The International Journal of Advanced Manufacturing Technology* 22 (2003) 54–67. [doi:10.1007/s00170-002-1442-8](https://doi.org/10.1007/s00170-002-1442-8).
- [2] D. F. Rogers, *An Introduction to NURBS: With Historical Perspective*, Morgan Kaufmann, 2001. [doi:10.1016/B978-1-55860-669-2.X5000-3](https://doi.org/10.1016/B978-1-55860-669-2.X5000-3).
- [3] S. Wang, Y. Xia, L. You, J. Zhang, PDE-based surface reconstruction in automotive styling design, *Multimedia Tools and Applications* 82 (2023) 1185–1202. [doi:10.1007/s11042-022-13297-x](https://doi.org/10.1007/s11042-022-13297-x).

- [4] S. Wang, N. Xiang, Y. Xia, L. You, J. Zhang, Real-time surface manipulation with C^1 continuity through simple and efficient physics-based deformations, *The Visual Computer* 37 (9-11) (2021) 2741–2753. [doi:10.1007/s00371-021-02169-4](https://doi.org/10.1007/s00371-021-02169-4).
- [5] D. Terzopoulos, Multilevel reconstruction of visual surfaces: Variational principles and finite-element representations, in: A. Rosenfeld (Ed.), *Multiresolution Image Processing and Analysis*, Springer, Berlin, Heidelberg, 1984, pp. 237–310. [doi:10.1007/978-3-642-51590-3_17](https://doi.org/10.1007/978-3-642-51590-3_17).
- [6] I. Kovács, T. Várady, Constrained fitting with free-form curves and surfaces, *Computer-Aided Design* 122 (2020) 102816. [doi:10.1016/j.cad.2020.102816](https://doi.org/10.1016/j.cad.2020.102816).
- [7] G. Hu, H. Cao, X. Qin, Construction of transition surfaces with minimal generalized thin-plate spline-surface energies, *Computational and Applied Mathematics* 41 (2022) 317. [doi:10.1007/s40314-022-02032-9](https://doi.org/10.1007/s40314-022-02032-9).
- [8] D. Mosbach, K. Schladitz, B. Hamann, H. Hagen, A local approach for computing smooth B-Spline surfaces for arbitrary quadrilateral base meshes, *Journal of Computing and Information Science in Engineering* 22 (1) (2022) 011003. [doi:10.1115/1.4051121](https://doi.org/10.1115/1.4051121).
- [9] D. Holz, S. R. Jeske, F. Lössner, J. Bender, Y. Yang, S. Andrews, Multiphysics simulation methods in computer graphics, *Computer Graphics Forum* 44 (2) (2025) e70082. [doi:10.1111/cgf.70082](https://doi.org/10.1111/cgf.70082).
- [10] A. Longva, F. Lössner, T. Kugelstadt, J. A. Fernández-Fernández, J. Bender, Higher-order finite elements for embedded simulation, *ACM Transactions on Graphics (TOG)* 39 (6) (2020) 1–14. [doi:10.1145/3414685.3417853](https://doi.org/10.1145/3414685.3417853).
- [11] H. P. Moreton, Minimum curvature variation curves, networks, and surfaces for fair free-form shape design, Ph.D. thesis, EECS Department, University of California, Berkeley (Mar 1993).
- [12] G. Celniker, D. Gossard, Deformable curve and surface finite-elements for free-form shape design, in: *Proceedings of the 18th Annual Conference on Computer Graphics and Interactive Techniques, SIGGRAPH '91*, Association for Computing Machinery, New York, NY, USA, 1991, pp. 257–266. [doi:10.1145/122718.122746](https://doi.org/10.1145/122718.122746).

- [13] R. Levien, C. H. Séquin, [Interpolating splines: Which is the fairest of them all?](#), *Computer-aided Design and Applications* 6 (2009) 91–102. URL <https://api.semanticscholar.org/CorpusID:15006988>
- [14] H. P. Moreton, C. H. Séquin, Functional optimization for fair surface design, in: *Proceedings of the 19th Annual Conference on Computer Graphics and Interactive Techniques, SIGGRAPH '92*, Association for Computing Machinery, New York, NY, USA, 1992, pp. 167–176. doi:[10.1145/133994.134035](https://doi.org/10.1145/133994.134035).
- [15] R. L. Harder, R. N. Desmarais, Interpolation using surface splines, *Journal of aircraft* 9 (2) (1972) 189–191. doi:[10.2514/3.44330](https://doi.org/10.2514/3.44330).
- [16] F. Bookstein, Principal warps: thin-plate splines and the decomposition of deformations, *IEEE Transactions on Pattern Analysis and Machine Intelligence* 11 (6) (1989) 567–585. doi:[10.1109/34.24792](https://doi.org/10.1109/34.24792).
- [17] J. Zhao, H. Zhang, Thin-plate spline motion model for image animation, in: *Proceedings of the IEEE/CVF conference on computer vision and pattern recognition*, 2022, pp. 3657–3666.
- [18] M. D. Buhmann, Radial basis functions, *Acta numerica* 9 (2000) 1–38. doi:[10.1017/S0962492900000015](https://doi.org/10.1017/S0962492900000015).
- [19] J. C. Carr, R. K. Beatson, J. B. Cherrie, T. J. Mitchell, W. R. Fright, B. C. McCallum, T. R. Evans, Reconstruction and representation of 3d objects with radial basis functions, in: *Proceedings of the 28th Annual Conference on Computer Graphics and Interactive Techniques, SIGGRAPH '01*, Association for Computing Machinery, New York, NY, USA, 2001, pp. 67–76. doi:[10.1145/383259.383266](https://doi.org/10.1145/383259.383266).
- [20] C. Chen, Y. Li, A robust method of thin plate spline and its application to dem construction, *Computers & Geosciences* 48 (2012) 9–16. doi:[10.1016/j.cageo.2012.05.018](https://doi.org/10.1016/j.cageo.2012.05.018).
- [21] Z. Majdisova, V. Skala, Big geo data surface approximation using radial basis functions: A comparative study, *Computers & Geosciences* 109 (2017) 51–58. doi:[10.1016/j.cageo.2017.08.007](https://doi.org/10.1016/j.cageo.2017.08.007).

- [22] M. I. G. Bloor, M. J. Wilson, Generating blend surfaces using partial differential equations, *Computer-Aided Design* 21 (3) (1989) 165–171. doi:[10.1016/0010-4485\(89\)90071-7](https://doi.org/10.1016/0010-4485(89)90071-7).
- [23] M. I. G. Bloor, M. J. Wilson, Using partial differential equations to generate free-form surfaces, *Computer-Aided Design* 22 (4) (1990) 202–212. doi:[10.1016/0010-4485\(90\)90049-1](https://doi.org/10.1016/0010-4485(90)90049-1).
- [24] H. Fu, S. Bian, E. Chaudhry, S. Wang, L. You, J. J. Zhang, PDE surface-represented facial blendshapes, *Mathematics* 9 (22) (2021) 2905. doi:[10.3390/math9222905](https://doi.org/10.3390/math9222905).
- [25] S. Wang, R. Wang, Y. Xia, Z. Sun, L. You, J. Zhang, Multi-objective aerodynamic optimization of high-speed train heads based on the PDE parametric modeling, *Structural and Multidisciplinary Optimization* 64 (2021) 1285–1304. doi:[10.1007/s00158-021-02916-0](https://doi.org/10.1007/s00158-021-02916-0).
- [26] S. Roberts, M. Hegland, I. Altas, Approximation of a thin plate spline smoother using continuous piecewise polynomial functions, *SIAM Journal on Numerical Analysis* 41 (1) (2003) 208–234. doi:[10.1137/S0036142901383296](https://doi.org/10.1137/S0036142901383296).
- [27] M. Bergou, M. Wardetzky, S. Robinson, B. Audoly, E. Grinspun, Discrete elastic rods, in: *ACM SIGGRAPH 2008 Papers, SIGGRAPH '08*, Association for Computing Machinery, New York, NY, USA, 2008, pp. 1–12. doi:[10.1145/1399504.1360662](https://doi.org/10.1145/1399504.1360662).
- [28] V. Romero, M. Ly, A. H. Rasheed, R. Charrondière, A. Lazarus, S. Neukirch, F. Bertails-Descoubes, Physical validation of simulators in computer graphics: a new framework dedicated to slender elastic structures and frictional contact, *ACM Trans. Graph.* 40 (4) (2021). doi:[10.1145/3450626.3459931](https://doi.org/10.1145/3450626.3459931).
- [29] J. P. M. d. Almeida, J. Reis, An efficient methodology for stress-based finite element approximations in two-dimensional elasticity, *International Journal for Numerical Methods in Engineering* 121 (20) (2020) 4649–4673. doi:[10.1002/nme.6458](https://doi.org/10.1002/nme.6458).
- [30] J. P. M. d. Almeida, E. A. W. Maunder, *Equilibrium Finite Element Formulations*, John Wiley & Sons, 2017. doi:[10.1002/9781118925782](https://doi.org/10.1002/9781118925782).

- [31] K. Olesen, B. Gervang, J. N. Reddy, M. Gerritsma, A higher-order equilibrium finite element method, *International Journal for Numerical Methods in Engineering* 114 (12) (2018) 1262–1290. doi:[10.1002/nme.5785](https://doi.org/10.1002/nme.5785).
- [32] I. Orynyak, K. Danylenko, Method of matched sections as a beam-like approach for plate analysis, *Finite Elements in Analysis and Design* 230 (2024) 104103. doi:[10.1016/j.finel.2023.104103](https://doi.org/10.1016/j.finel.2023.104103).
- [33] I. Orynyak, A. Tsybulnyk, K. Danylenko, Spectral realization of the method of matched sections for thin-plate vibration, *Archive of Applied Mechanics* 95 (2025) 51. doi:[10.1007/s00419-024-02755-7](https://doi.org/10.1007/s00419-024-02755-7).
- [34] I. Orynyak, A. Tsybulnyk, K. Danylenko, A. Oryniak, S. Radchenko, Timestep-dependent element interpolation functions in the method of matched sections on the example of heat conduction problem, *Journal of Computational and Applied Mathematics* 456 (2025) 116222. doi:[10.1016/j.cam.2024.116222](https://doi.org/10.1016/j.cam.2024.116222).
- [35] K. Danylenko, I. Orynyak, Numeric analysis of elastic plane body static problem by the method of matched sections, *Mechanics and Advanced Technologies* 8 (4(103)) (2024) 428–440. doi:[10.20535/2521-1943.2024.8.4\(103\).313412](https://doi.org/10.20535/2521-1943.2024.8.4(103).313412).
- [36] F. Leckie, E. Pestel, Transfer-matrix fundamentals, *International Journal of Mechanical Sciences* 2 (3) (1960) 137–167. doi:[10.1016/0020-7403\(60\)90001-1](https://doi.org/10.1016/0020-7403(60)90001-1).
- [37] R. Li, B. Wang, G. Li, Benchmark bending solutions of rectangular thin plates point-supported at two adjacent corners, *Applied Mathematics Letters* 40 (2015) 53–58. doi:[10.1016/j.aml.2014.09.012](https://doi.org/10.1016/j.aml.2014.09.012).
- [38] Y. Yi, Z. Tang, C. Liu, Progressive iterative approximation for extended B-Spline interpolation surfaces, *Mathematical Problems in Engineering* 2021 (2021) 5556771. doi:[10.1155/2021/5556771](https://doi.org/10.1155/2021/5556771).